Article

Nearly 90% Circularly-Polarized Emission in Monolayer WS<sub<i></i>>2</sub> Single Crystals by Chemical Vapor Deposition

Wei-Hsiang Lin, Wei-Shiuan Tseng, Cora M. Went, Marcus L Teague, George R. Rossman, Harry A Atwater, and Nai-Chang Yeh

ACS Nano, **Just Accepted Manuscript** • DOI: 10.1021/acsnano.9b05550 • Publication Date (Web): 23 Aug 2019

Nearly 90% Circularly-Polarized Emission in Monolayer WS_2 Single Crystals by Chemical Vapor Deposition

Wei-Hsiang Lin,[†] Wei-Shiuan Tseng,[‡] Cora M. Went,[‡] Marcus L. Teague,[‡] George. R. Rossman,[§] Harry A. Atwater[†,∥] and Nai-Chang Yeh[*‡,∥]

[*]Corresponding author, ncyeh@caltech.edu

[†]Department of Applied Physics, California Institute of Technology, Pasadena, CA 91125, USA

[‡]Department of Physics, California Institute of Technology, Pasadena, CA 91125, USA

[§]Division of Geological and Planetary Sciences, California Institute of Technology, Pasadena, A 91125, USA

[∥]Kavli Nanoscience Institute, California Institute of Technology, Pasadena, CA 91125, USA

ABSTRACT:

Monolayer transition-metal dichalcogenides (TMDCs) in the 2H-phase are semiconductors promising for opto-valleytronic and opto-spintronic applications because of their strong spin-valley coupling. Here we report detailed studies of opto-valleytronic properties of heterogeneous domains in CVD-grown monolayer WS_2 single crystals. By illuminating WS_2 with off-resonance circularly-polarized light and measuring the resulting spatially resolved circularly-polarized emission (P_{circ}), we find significantly large circular polarization (P_{circ} up to 60% and 45% for α- and β-domains, respectively) already at 300 K, which increases to nearly 90% in the α-domains at 80 K. Studies of spatially resolved

photoluminescence (PL) spectroscopy, Raman spectroscopy, x-ray photoelectron spectroscopy (XPS), Kelvin-probe force microscopy (KPFM) and conductive atomic force microscopy (CAFM) reveal direct correlation among the PL intensity, defect densities and chemical potential, with the α-domains showing lower defect densities and a smaller work function by 0.13 eV than the β-domains. This work function difference indicates the occurrence of type-two band alignments between the α- and β-domains. We adapt a classical model to explain how electronically active defects may serve as non-radiative recombination centers, and find good agreement between experiments and the model. Scanning tunneling microscopic/spectroscopic (STM/STS) studies provide further evidences for tungsten vacancies (WVs) being the primary defects responsible for the suppressed PL and circular polarization in WS_2. These results therefore suggest a pathway to control the opto-valleytronic properties of TMDCs *via* defect engineering.

KEYWORDS: transition metal dichalcogenides, WS_2, CVD, KPFM, CAFM, STM, valley polarization

There has been a surge of intense research efforts on two-dimensional (2D) van der Waals (vdW) materials because of their interesting properties and great promise for technological applications.[1-4] These 2D materials, such as semi-metallic graphene,[5-9] insulating h-BN,[10-14] and semiconducting transition metal dichalcogenides (TMDCs),[15-19] can be synthesized on a wafer scale by chemical vapor deposition (CVD), which provides a feasible route towards practical applications. The electrical and optical properties of TMDCs can be significantly affected by crystal imperfections such as vacancies, impurities and grain boundaries.[20-22] In particular, vacancies in TMDCs appear to be unpreventable and are naturally formed inside the single crystalline grains during the CVD growth process. Such vacancies can be primary contributors to carrier scattering, doping effects and varying optical properties in these materials.

Among TMDCs in the 2H-phase, monolayer tungsten disulfide (WS_2) consists of a plane of tungsten atoms sandwiched between top and bottom sulfur layers. It has been found that atomic vacancies of tungsten and sulfur are common occurrences in WS_2, and that the electrical and optical properties of a given WS_2 monolayer are dominated by the type of vacancies because of differences in the defect states. For instance, monolayer

hexagonal-shape WS_2 (h-WS_2) flakes with triangular heterogeneous defect domains have been synthesized by CVD under hydrogen-rich growth conditions, as reported by several research groups.[23-27] Curiously, the optical emission in the h-WS_2 flakes exhibits alternating areas of bright and dark photoluminescence (PL) emission within each h-WS_2 flake, and the resulting PL image looks similar to the radioactive hazard symbol, as exemplified by the left panel of Figure 1a. According to previous studies,[23-27] the α-domains with a stronger PL intensity and higher mobility are associated with W-edges and S-vacancies (SVs), and the β-domains with a significantly quenched PL intensity and lower electron mobility exhibit a blue-shifted PL peak position, and are associated with S-edges and W-vacancies (WVs). A schematic illustration of the heterogeneous defect domains for WVs and SVs in a single crystalline h-WS_2 is shown in the right panel of Figure 1a.

Similar to other monolayer TMDCs in the 2H-phase, monolayer WS_2 is an ideal candidate for valleytronic applications due to its inequivalent K and K′ valleys at the edge of the Brillouin zone.[28-29] Because of strong spin-orbit coupling and time-reversal symmetry, the valence bands (VB) in the K (K′) valley have a large energy spin splitting

of ~ 420 meV for WS_2[28-29] between the top spin-up (spin-down) band and the bottom spin-down (spin-up) band. This difference results in valley-dependent optical selection rules: circularly polarized light with positive helicity (σ+) couples to the K valley and the negative helicity (σ–) couples to the K′ valley.[30-32] It is therefore possible to selectively populate and manipulate the different valleys (K or K′) by means of circularly polarized light.

When monolayer WS_2 is illuminated with circularly polarized light of photon energies larger than the energy gap, excitons (*i.e.*, bound electron-hole pairs) are created in a single valley. The radiative decay of excitons within this valley subsequently generates circularly polarized light due to the optical selection rules. Therefore, measuring the circular polarization of photoluminescence (PL) provides a direct means to monitor the valley population. Valley populations will also be affected by intervalley scattering, a process that may be enabled by Coulomb interactions or impurity/phonon scattering.[33-36] At high temperatures or under a sufficiently high photon-excitation energy, large phonon populations will couple to the valleys, thereby reducing the valley specific populations. To date, most reports of circularly polarized PL spectra[37-41] have only been observed in

systems measured at relatively low temperatures (< 30 K) or near the resonant excitation condition.

Here we report successful CVD growth (Figure S1) of monolayer h-WS_2 that exhibits significant circular polarization already at room temperature and nearly 90% circular polarization (CP) in the α-domains at 80 K without the resonant excitation condition. Detailed characterizations by Raman spectroscopy, PL, X-ray photoemission spectroscopy (XPS) and conducting atomic force microscopy (CAFM) revealed that these h-WS_2 samples were of high quality, large domains and low defect densities. Additionally, systematic studies of monolayer h-WS_2 by spatially resolved PL maps and point spectra of polarized PL emission were made on the α- and β-domains of h-WS_2 at both room temperature and low temperature (80K). We found that at room temperature, the PL spectra of neutral excitons exhibited a CP of ~ 50% and ~ 40% in the α- and β-domains, respectively. Moreover, the degree of circularly polarized emission in α-domains approached ~ 90% at 80K, suggesting nearly perfect valley polarization. Spatially-resolved CAFM studies revealed that the areal defect density was on the order of 10^{10} cm^{-2} in the α-domains and on the order of 10^{11} cm^{-2} in the β-domains. Following a similar

analysis in Refs. 42 and 51, we related the areal defect density in each domain to the corresponding PL intensity and obtained an estimate for the non-radiative recombination lifetime.[42,51] Additionally, spatially resolved studies using Kelvin-probe force microscopy (KPFM) found that the work function in the β-domains was consistently larger than that in the α-domains by 0.15 eV, suggesting type-2 semiconducting band alignments along the domain boundaries that are favorable for stabilizing interfacial excitons.[52] Atomically resolved imaging and spectroscopic studies by scanning tunneling microscopy (STM) further revealed that the non-radiative defects were primarily associated with the WVs rather than SVs, consistent with the CAFM findings in regions of higher defect densities. Our results thus provide direct evidences for WVs being the primary non-radiative recombination sites in h-WS_2 that are responsible for the suppression of PL intensity and circular polarization.

RESULTS AND DISCUSSION

Monolayer h-WS_2 samples were synthesized on SiO_2 (300 nm)/Si substrates by means of CVD, as schematically shown in Figures S1 and S2. The hexagonal flakes typically had lateral dimensions on the order of several tens to hundreds of micrometers so that

optical studies at many discrete locations across a single flake could be carried out. Further details for the h-WS_2 growth processes are described in Methods and Supplementary Information Note 1.

Our monolayer h-WS_2 samples exhibited typical fluorescence images analogous to the radioactive hazard symbol, as mentioned in the introduction and exemplified in Figure 1a. Spatially resolved topographic studies on the same samples using atomic force microscopy (AFM) revealed smooth topographic maps (Figure 1b). Specifically, while the height difference between the WS_2 single crystal and the SiO_2/Si substrate was ~ 0.85 nm, which was consistent with the monolayer thickness of WS_2, there was no discernible height differences between the two domains of different PL intensities (Figure 1d). Spatially resolved measurements of the AFM phase mode revealed a clear phase difference (1º) between the two domains (Figure 1c), and the resulting phase map correlated well with the pattern shown in Figure 1d. Similarly, spatially resolved Raman spectroscopic maps for the A_{1g} and E^1_{2g} modes of a monolayer h-WS_2 single crystal (shown respectively in Figures 1e and 1f) also exhibited the same pattern.

Figure 1g shows a representative PL spectrum from 1.96 eV to 2.01eV for the typical A-exciton peak of h-WS_2. The A-exciton PL peak for the α-domain is redshifted compared to that of the β-domain. This redshift may be attributed to tensile strain existed in the α-domains and/or to a higher carrier density. Moreover, the PL intensity in the α-domains is always enhanced by about one order of magnitude when compared with the β-domains.

Generally speaking, the PL intensity can be modulated by a variety of factors such as stoichiometry, strain, doping and density of non-radiative recombination centers. To investigate the contributions from strain and doping effects, we performed Raman intensity and frequency mapping of the A_{1g} and E^1_{2g} modes, which displayed contrast between the α- and β-domains (Figures 1e-f) and were similar to the PL mapping (Figure 1d). We found that the strain-related E^1_{2g} mode exhibited a redshift in the α-domain relative to the β-domain (0.5 cm^{-1}), indicating a tensile-strain effect. Similarly, the redshift (1.2 cm^{-1}) of the doping-related A_{1g} mode in the α-domain relative to the β-domain implied carrier doping effects (Figure 1h), which was consistent with the observed PL redshift (Figure 1g). The LA (M) mode at 176 cm^{-1}, which is associated with the longitudinal acoustic

phonon at the M point of the Brillouin zone, may be considered as a useful indicator of the sample quality. Specifically, a finite intensity of the LA (M) mode implies the presence of defects or disorder that satisfied the q = 0 Raman selection rule. Additionally, the intensity of the LA (M) mode, I(LA), may be related to the inter-defect spacing (L_D) [43] by the expression $I(\mathrm{LA}) \propto L_D^{-2}$. Figure S3 demonstrates that the intensity of the LA (M) mode associated with the β-domain was shown to be larger than that of the α-domain, implying a shorter inter-defect distance and therefore a higher areal density of disorder in the β-domain that signifies more non-radiative recombination centers and a reduced PL intensity.

In addition to the PL/Raman spectroscopic studies, spatially-resolved X-ray photoelectron emission spectroscopy (XPS) was carried out on monolayer WS_2 transferred to Au (111) / mica substrates (Figure 2a) to probe the chemical composition and stoichiometry of the h-WS_2 single crystal. High-resolution XPS mapping performed on the h-WS_2 samples revealed apparent hexagonal geometry, as exemplified in Figure S4a. Photoelectrons from core level of W and S atoms were acquired from both α- and

β-domains. As shown in Figures 2b and 2c, the corresponding binding energies in the α-domain (β-domain) were 34.31 eV (34.44 eV) for $W_{4f\ 5/2}$, 32.15 eV (32.28 eV) for $W_{4f\ 7/2}$, 162.87 eV (162.9 eV) for $S_{2p3/2}$, and 163.07 eV (163.1 eV) for $S_{2p1/2}$. Considering the error range of $\pm$0.025 eV for the binding energies determined using our XPS system, the upshift in the α-domain binding energies (~ 0.13 eV) relative to those in the β-domain was prominent for the W-4f peaks, in good agreement with the valance-band maximum shift due to doping-induced Fermi level modulation. In contrast, the upshift of the S-2p peaks (~ 0.03 eV) was much smaller and essentially negligible given the error range of our XPS system. This negligible upshift of the S-2p peaks in the α-domain may be attributed to the tensile strain effect that affected the S-2p valence electrons more significantly, which contributed to a binding-energy downshift that compensated the doping-induced binding energy upshift. On the other hand, the tensile strain had much weaker effects on the W-4f core electrons so that the doping-induced energy upshifts prevailed for the W-4f peaks in the α-domain.

We have also explored the surface potential (work function) of the α- and β-domains *via* Kelvin probe force microscopy (KPFM) because the work functions of semiconductor

2D materials are sensitive to the corresponding variable Fermi level. To determine the work function of the Al-coated AFM tip, we first performed UPS measurements on the Au (111) / mica sample, which found the work function of Au (111) to be 4.8 eV, as shown in Figure S4b. Next, we performed KPFM measurements using the Al-coated AFM tip on Au (111) / mica, which yielded the value of the contact potential difference (V_{CPD}^{0}) between the Al-coated AFM tip and Au (111), where the contact potential difference (V_{CPD}^{0}) was defined as the difference between the work function of the tip (ϕ_{tip}) and that of Au (111), so that $eV_{\mathrm{CPD}}^{0} = \phi_{\mathrm{tip}} - 4.8\,\mathrm{eV}$. Finally, KPFM measurements using the Al-coated AFM tip on h-WS_2 yielded the contact potential difference (V_{CPD}) between the Al-coated AFM tip and different domains of the h-WS_2 sample so that we obtained the following relation:

$$eV_{\mathrm{CPD}} = \phi_{\mathrm{tip}} - \phi_{\mathrm{WS_2}}, \quad \Rightarrow \quad \phi_{\mathrm{WS_2}} = \phi_{\mathrm{tip}} - eV_{\mathrm{CPD}}, \tag{1}$$

where $\phi_{\mathrm{WS_2}}$ is the work function of the WS_2 sample. From spatially resolved measurements of V_{CPD}, the work function difference between the α- and β-domains can be determined, and the resulting KPFM images are shown in Figures 2d and 2e.

A schematic representation of the band diagram with the Fermi levels for the α- and β-domains relative to the vacuum level is shown in Figure 2f. The difference in the Fermi levels between the α- and β-domains can be calculated directly from V_{CPD} using the following equation:

$$\Delta E_f = E_{f,\alpha} - E_{f,\beta} = eV_{\mathrm{CPD},\alpha} - eV_{\mathrm{CPD},\beta} = e\Delta V_{\mathrm{CPD}} = \left(\phi_\beta - \phi_\alpha\right), \quad (2)$$

where $E_{f,\alpha}(\phi_\alpha)$ and $E_{f,\beta}(\phi_\beta)$ are the Fermi levels (work functions) of the α- and β-domains, respectively. Interesting, we note that the band diagram at the interface of the α- and β-domains is consistent with a type-2 band alignment that supports long-lived interfacial excitons.[52]

To investigate the degree of valley polarization in our monolayer h-WS_2, we performed polarization-resolved PL spectroscopy measurements at both room temperature and 80 K under the excitation of a 514 nm continuous-wave laser source, as schematically illustrated in Figure 3a.

For spatially-resolved PL mapping, the sample was excited with σ_+ helicity and the laser was scanned across a (13 μm × 13 μm) area at a step size of 0.2 μm. The detection optics

were set first for the σ_+ analysis and then for the σ_- analysis over the same area in two separate scans. The energy of the PL peak within the range of 1.9 eV to 2.1 eV for the σ_+ (σ_-) detection was determined, and the PL intensity map taken at the peak energy is shown in Figure 3b for the σ_+ detection and in Figure 3c for the σ_- detection, both obtained at room temperature (RT). These PL maps reveal the same emission pattern as the unpolarized excitation. This type of PL pattern, with lower PL intensity in the β-domain and higher PL intensity in the α-domain (about 10 times stronger than that in the β-domain), was common among all monolayer h-WS_2 single crystals that we synthesized.

Given the polarization-resolved PL intensities $I(\sigma_+)$ and $I(\sigma_-)$, the degree of circular polarization (P_{circ}) is define by the following expression:

$$P_{\text{circ}} = \frac{I(\sigma_+) - I(\sigma_-)}{I(\sigma_+) + I(\sigma_-)}. \quad (3)$$

Using Eq. (3), the degree of circular polarization across a monolayer h-WS_2 crystal was obtained and is illustrated in Figure 3d. The higher degree of polarization (DOP) in the α-domain (45% ~ 60%) and lower DOP in the β-domain (20% ~ 45%) was found to be well

correlated to the PL intensity pattern. Similar results were also obtained for polarization-resolved mapping acquired with the σ_- excitation, as shown in Figure S5.

The PL spectra of the α-domain (Figure 3e) and the β-domain (Figure 3f) taken at RT both displayed a single peak with the maximum intensity at 1.92 eV, indicating that the RT emission characteristics were dominated by the neutral excitons. These neutral excitons exhibited very large circular polarization at both the α-domain (P_{circ} ~ 50%) and β-domain (P_{circ} ~ 40%) of our h-WS_2 samples even at RT, in stark contrast to recent reports by other groups (with P_{circ} = 0.2% ~ 32%) on monolayer WS_2,[40-42] as summarized in Table S2. The PL peak for both domains was found to slightly blue-shift to 1.96 eV at a lower temperature (LT) 80 K. As exemplified in Figure 3g, the LT (80 K) PL intensity of the σ_+ detection at the α-domain increased threefold relative to the corresponding RT signals, whereas the PL intensity of the σ_- detection remained the same at 80 K. In particular, the DOP at the α-domain approached nearly 90% at 80 K. In contrast, the LT (80K) PL spectra at the β-domain revealed that the PL intensities for both the σ_+ and σ_- detections increased tenfold relative to the corresponding PL spectra at RT, as

exemplified by Figure 3h. However, the DOP of the β-domain at 80 K remained largely the same as that at RT.

Our finding of significant disparity in the DOP enhancement with decreasing temperature for two different domains is quite unusual: while the common observation of increasing PL intensity with decreasing temperature may be attributed to the reduction of thermally activated non-radiative recombination, this mechanism should have resulted in a comparable enhancement factor with decreasing temperature for the PL intensity in the same material. However, the enhancement factor for the PL intensity at LT was apparently different in different domains of the h-WS_2 single crystal, which led to significantly different DOP at LT. A feasible explanation for such disparity in the DOP enhancement with decreasing temperature may be due to negligible non-radiative recombination centers for excitons in the α-domain as opposed to more non-radiative recombination centers in the β-domain. To shed light on this issue, we performed spatially-resolved conductive atomic force microscope (CAFM) measurements to be detailed below, which facilitated precise identifications of defects that could serve as the

non-radiative recombination centers and also provided direct quantifications of the areal defect density.

A schematic illustration of the experimental configuration for the conductive atomic force microscope (CAFM) measurements is shown in Figure 4a, where all data acquisition was done at RT in air. It is worth noting that careful sample preparation for the CAFM measurements was critically important to obtaining reproducible results. In particular, an atomically flat conductive substrate for the monolayer h-WS_2 sample was necessary. For this purpose, we first transferred a thick piece of CVD-grown graphite onto an atomically flat Au (111) (200 nm) / mica substrate, followed by a monolayer of h-WS_2 transferred from its CVD growth substrate onto the graphite/Au (111)/mica substrate. After the transfer, we annealed the combined sample-on-substrate in a hydrogen-argon gas mixture (with a ratio of H_2 to Ar of 1 to 3) for 3 hours to remove possible contaminants and wrinkles, which helped improve the contact uniformity between the monolayer h-WS_2 and the graphite substrate. Details of the h-WS_2 transfer and the annealing processes can be found in Methods and Supplementary Information. Lastly, a voltage was applied to the sample lead so that a current flowed between the Pt/Ir coated CAFM tip and the

sample, and this current was recorded by a current amplifier. By scanning the AFM tip across the sample and recording the currents at each pixel with a pixel spacing of 0.9 nm, we obtained spatially resolved CAFM maps over different domains of the h-WS_2 sample.

In these CAFM maps, the locations of defects were easily identified as distinct high-current features: the defect locations generally exhibited more than 2 orders of magnitude higher currents than areas without defects. Additionally, the electrical characteristics of each defect could be well quantified by measurements of the current-voltage (I-V) curves, as exemplified in Figure 4b by the comparison of a typical I-V curve obtained on a defect with a reference I-V curve obtained away from any defects. The I-V curve associated with a defect exhibited much enhanced currents at bias voltages $|V| > 0.3$ V and was nearly symmetric about zero applied bias. These defect sites were generally much more conductive than regions without defects, as demonstrated by the comparison of the differential conductance taken on and off defects in the inset of Figure 4b.

In Figures 4d-i, spatially-resolved CAFM differential conductance maps taken at a bias voltage of 0.9 V are shown over different 1 μm × 1 μm areas at locations specified on the h-WS_2 single crystal in Figure 4c, which shows a spatial map of PL intensity taken on the

sample after its transfer onto the substrate for the CAFM measurements. The apparent visibility of defect locations in the CAFM maps enabled direct counting of the number of the defects in both the α- and β-domains. Specifically, for the α-domain, we found 149 defects in Figure 4d, which corresponded to a defect density of 1.49×10^{10} cm^{-2}. Similarly, we obtained 175 defects (1.75×10^{10} cm^{-2}) in Figure 4e, and 359 defects (3.59×10^{10} cm^{-2}) in Figure 4f. For the β-domain, we found 822 defects (8.22×10^{10} cm^{-2}) in Figure 4g, 1370 defects (1.37×10^{11} cm^{-2}) in Figure 4h, and 1750 defects (1.75×10^{11} cm^{-2}) in Figure 4i. These CAFM measurements clearly indicated that the areal density of these highly conductive defect sites was about one order of magnitude higher in the β-domain than in the α-domain.

Here we emphasize that other types of defects not detectable by the CAFM measurements may exist, and in this work we only consider one specific type of defects that are most electrically active and correlate their densities with the corresponding spatially-resolved PL. In Figure 4j we compare the defect density and the PL intensity as a function of the position numerated along a line in Figure 4c, and find that the measured defect density generally anti-correlates with the PL intensity for both α- and β-domains.

A major challenge to understanding the excitonic behavior in h-WS_2 is the wide variety of mechanisms that can affect the exciton recombination, including substrate effects, defect related recombination and other non-radiative recombination pathways[44-51]. From our experiments, the apparent anti-correlation between the defect density and the PL intensity is helpful in identifying the role of defects in the exciton recombination for monolayer h-WS_2.

Generally speaking, the PL intensity is proportional to the PL quantum yield (QY) of excitons, and a standard QY is defined by the following expression:

$$\mathrm{QY} \equiv \tau_r^{-1} \Big/ \left(\tau_r^{-1} + \tau_{nr}^{-1} \right), \tag{4}$$

where τ_r (τ_{nr}) is the average radiative (non-radiative) recombination time of excitons. Typically the non-radiative recombination rate τ_{nr}^{-1} may be further divided into two components if we assume that excitons do not interact with each other. That is,

$$\tau_{nr}^{-1} = \tau_{nr,sub}^{-1} + \tau_{nr,defect}^{-1}, \tag{5}$$

where $\tau_{nr,sub}$ is the average non-radiative recombination time for substrate related effects, which may also include any other non-radiative recombination mechanisms, and $\tau_{nr,defect}$ is the average non-radiative recombination time for defect-related effects.

To understand the correlation between the defect density and PL intensity, we followed a similar analysis by Rosenberger *et al.*[42] Specifically, we assumed that the defect-related non-radiative recombination occurred when excitons collided with defects and resulted in non-radiative recombination. For an exciton with an effective collision radius r traveling with a speed v, an area swept by the exciton over a time period t in the 2D sheet with a defect density n_d would result in N collisions, where $N = n_d(2rvt)$. Therefore, the collision time $\tau_{nr,defect}$ between the exciton and defects can be defined by the following expression:

$$\tau_{nr,defect} = \frac{t}{N} = \frac{t}{n_d\left(2rvt\right)} = \frac{1}{2rvn_d}, \quad \Rightarrow \quad \tau_{nr,defect}^{-1} = 2rvn_d. \tag{6}$$

Combining Eqs. (4)-(6) and assuming that the QY and the empirical PL intensity, $(PL)_{\text{exp}}$, are related by a scaling coefficient C, we arrived at the following relation:[42]

$$(PL)_{\text{exp}} = C\frac{\tau_r^{-1}}{\tau_r^{-1} + \tau_{nr,sub}^{-1} + 2rvn_d}. \tag{7}$$

Empirically, the values of τ_r in different domains could be directly determined from time resolved PL (TRPL), which yielded τ_r = 1.5 ns in the α-domain and τ_r = 230 ps in the β-domain for monolayer h-WS_2. These values were consistent with the range of 0.2 ~ 4 ns reported in the literature for monolayer WS_2.[43,48,50] If we further assumed that a thermal speed of excitons at room temperature (RT) of v = 10^5 m/s,[53,54] and an effective collision radius r = 2.1 nm based on previous reports,[54] we obtained in Figure 4k the relation between the spatially varying PL intensity of a monolayer h-WS_2 on graphite/Au (111)/mica and the corresponding local defect density. The solid black line represents the fitting curve for the PL measurements using Eq. (7) with the fitting parameters C = 3.1×10^5 and $\tau_{nr,sub}$ = 30 ps. These fitting parameters were consistent for both domains in h-WS_2, which implies that our direct quantification of the defect density n_d helped decouple the defected-related non-radiative recombination (associated with $\tau_{nr,defect}^{-1} = 2rvn_d$) from other non-radiative mechanisms (associated with $\tau_{nr,sub}^{-1}$).

To understand why the DOP differed in the α- and β-domains, we considered a rate equation model in the steady state to find the relationship between the DOP and defect-

related non-radiative recombination. As detailed in Supplementary Information Note 6, the circular polarization P_{circ} for neutral excitons in the steady-state rate model can be given by the following expression:

$$P_{circ} = \frac{P_0(1-\delta)^2}{1+2\left(\tau_{ex}/\tau_{intervalley}\right)} = \frac{P_0\left[1-\left(\delta_{imp}+\delta_{phonon}\right)^2\right]}{1+2\left(\tau_{ex}/\tau_{intervalley}\right)} \ , \qquad (8)$$

where P_0 is the theoretical degree of circular polarization, τ_{ex} ($\tau_{intervalley}$) is the neutral exciton (intervalley) relaxation time, and $(1-\delta)$ represents the selectivity in the initial excitation with $0 < \delta < 1$.[32] In particular, we may express $\delta = \delta_{imp} + \delta_{phonon}$ to account for impurity/defects/substrate-related and phonon-assisted recombination effects that led to inter-valley mixing from finite-momentum scattering,[32] with $(1-\delta)$ decreasing with increasing scattering densities and increasing temperature. Thus, from Eq. (8) we expect P_{circ} to increase with either decrease in τ_{ex}, increase in $\tau_{intervalley}$, or decrease in δ. For both α- and β-domains of the same h-WS_2 sample, given that they were excited with the same laser power and wavelength, and were also exposed to the same ambient, we may assume that the optically generated exciton densities n_K^{ex} and $n_{K'}^{ex}$ were the same for both domains.

In monolayer TMDCs at RT, the non-radiative lifetimes may be several orders of magnitude shorter than the radiative lifetime so that the overall exciton lifetime is much reduced. From our CAFM measurements at RT and using Eqs. (6) – (7) to fit the PL intensities, we found that the α-domains with lower defect densities would exhibit higher PL intensities and longer non-radiative lifetimes (τ_{nr} = 4.7 ps ~ 10 ps for n_d = 3.59×10^{10} cm^{-2} ~ 1.49×10^{10} cm^{-2}), whereas the β-domains with higher defect densities would exhibit lower PL intensities and shorter non-radiative lifetimes (τ_{nr} = 1.1 ps ~ 2.6 ps for n_d = 1.75×10^{11} cm^{-2} ~ 8.22×10^{10} cm^{-2}). By considering the radiative (τ_r) and non-radiative (τ_{nr}) lifetimes of excitons in both domains, we could directly estimate the exciton lifetime τ_{ex} by the relation $\tau_{ex}^{-1} = \tau_r^{-1} + \tau_{nr}^{-1}$, which yielded larger values of τ_{ex} = 4.72 ps ~ 10 ps for the α-domains and smaller values of τ_{ex} = 1.1 ps ~ 2.6 ps for the β-domains at RT. Additionally, the large differences in the defect density between the α- and β-domains gave rise to lower selectivity (*i.e.*, smaller $(1-\delta)^2$) in the β-domains. Therefore, the nearly temperature independent P_{circ} in the β-domain may be understood in terms of the competing effects between increasing $(1-\delta)^2$ and decreasing $(\tau_{ex})^{-1}$ with decreasing

temperature according to Eq. (8). In contrast to the β-domain, $(\tau_{ex})^{-1}$ in the α-domain did not decrease as much with decreasing temperature due to far fewer non-radiative recombination sites, whereas the selectivity $(1-\delta)^2$ increased more significantly with decreasing temperature due to diminishing δ_{phonon} and negligible δ_{imp}. Therefore, the value of P_{circ} increased dramatically with decreasing temperature in the α-domains according to Eq. (8), consistent with our experimental finding.

While the temperature-dependent PL intensities and DOP in both the α- and β-domains of h-WS_2 can be consistently explained in terms of the differences in the density of electrically-active defects, the microscopic origin for these defects is not yet understood. By performing scanning tunneling microscopy (STM) measurement on monolayer WS_2 single crystals,[55,56] we obtained atomically spatial-resolved images associated with either the SVs (Figure 5a) or the WVs (Figure 5d).

For the SV sites of WS_2, as exemplified by the white dash triangles in Figure 5a, the corresponding tunneling conductance spectra were found to be comparable to those of vacancy-free regions. Specifically, both the tunneling current (I) *vs.* bias voltage (V) spectra and the corresponding (dI/dV)-*vs.*-V spectra taken at a SV (represented by the

red curves in Figures 5b and 5c for the SV location $\alpha 1$ shown in Figure 5a) is essentially indistinguishable from those taken at a vacancy-free region (represented by the orange curves in Figures 5b and 5c for the vacancy-free location $\alpha 2$ shown in Figure 5a). In particular, the (dI/dV) spectra revealed that the valence band maximum (VBM) and conduction band minimum (CBM) were located at E_{VBM} ~ −1.1 eV and E_{CBM} ~ +0.9 eV, respectively, yielding a band gap of $E_g = E_{CBM} - E_{VBM}$ = ~2 eV (Figure 5c). In contrast, for the WV sites as exemplified by the large white dashed triangle in the Figure 5d, the tunneling spectra taken at the WV sites β_1 and β_2, respectively illustrated by the blue and green curves in Figure 5e for the *I-vs.-V* spectra and in Figure 5f for the (dI/dV)-*vs.*-*V* spectra, revealed an enhance differential conductance at smaller biased voltages and a smaller bandgap of ~ 1.1eV, with the VBM and CBM move to ~ −0.8 eV and ~ +0.3 eV, respectively. These spectra associated with the WVs were qualitatively similar to the CAFM measurements in Figure 4b, even though direct quantitative comparison of the *tunneling* conductance data from STM with the *contact* conductance data derived from CAFM is not straightforward without detailed information and modeling of the nanoscale interfacial properties between the AFM tip and WS_2. Overall, the combined information

derived from atomically resolved STM studies and the nanoscale CAFM measurements strongly suggests that the WV sites rather than the SV sites in monolayer WS_2 are the primary non-radiative combination centers that are responsible for the reduction in the PL intensity and DOP.

The aforementioned scenario of a higher WV density in the β-domain is not only consistent with the observation of reduced PL intensities and DOP but also accounts for the larger work function in the β-domain (as found by the KPFM studies) because of the excess hole-doping associated with WVs in WS_2. Therefore, we have been able to provide a unified description for the varying chemical, electronic and optical properties of different domains in monolayer h-WS_2 in terms of the varying WV densities.

Finally, we note that a well-defined, net valley polarization can be established along the boundary between the α- and β-domains under circularly polarized light as the result of their different DOP. Hence, the domain boundaries in our monolayer h-WS_2 samples may be considered as one-dimensional *topological channels* so that a Hall bar device patterned along one of the domain boundaries is expected to exhibit CPL-induced valley Hall currents even at room temperature. Such opto-valleytronic and related opto-

spintronic phenomena for devices fabricated along the topological channels in monolayer h-WS_2 will be an interesting topic for future investigation.

CONCLUSION

In summary, our experimental investigations based on spatially resolved measurements of PL, Raman spectroscopy, XPS, KPFM, CAFM and STM have clarified the microscopic physical origin for markedly different reports of PL properties in CVD-grown monolayer WS_2 by attributing the differences to varying densities of tungsten vacancies (WVs) that act like non-radiative recombination centers. We have also demonstrated large circular polarizations in the PL spectra of our monolayer CVD-grown h-WS_2 single crystals under off-resonant illumination and at relatively high temperatures (from RT to 80 K) when compared with other TMDCs, as detailed in Tables S1 and S2 and summarized in Figure S7. The occurrence of type-two band alignments along the domain walls of h-WS_2 further promises longer exciton lifetimes along the domain boundaries. This work therefore suggests a pathway towards engineering valley

polarizations and exciton lifetimes in TMDCs by controlling the type and density of defects that serve as non-radiative exciton recombination sites.

METHODS

Sample preparation

Pre-treatment of SiO_2/Si substrate: SiO_2/Si substrates (300 nm SiO_2) were used for the CVD growth of WS_2. Prior to the growth, SiO_2/Si substrates were first soaked and sonicated in acetone and isopropyl alcohol (IPA) for 30 minutes to remove organic impurities, and then soaked in Nanostrip for 60 minutes, and finally washed with deionized water and dried with nitrogen gas.

Synthesis of mono- and multilayer WS_2: We used WO_3 and S as precursors in an atmospheric pressure CVD system to grow monolayer h-WS_2 on Si/SiO_2 substrates. A schematic drawing of the home-built CVD system is shown in Figure S1. Our setup includes the following parts: a quartz tube with a diameter of 1 inch and a length of 100 cm, a one-inch inner diameter (I.D.) horizontal split tube furnace (Lindberg Blue M), two mass flow controllers calibrated for Ar and H_2, with stainless steel flanges at both ends connected to a chiller water circulation system operating at 10 °C.

In the first step of the procedure, 95 mg WO_3 precursor mixed with 5mg KI was placed in a quartz boat containing the SiO_2/Si substrates set face-down directly above the W

source precursor, and the quartz boat was then positioned at the center of the furnace. A second boat containing 100 mg S (Alfa Aesar, 99.999+ %) was placed upstream at 16 cm away from the W source. Next, the system was pump down to 3×10^{-2} torr to eliminate air and moisture. After the system reached the base pressure, the Ar/H_2 (80/40 sccm) carrier gas was introduced until atmospheric pressure was achieved. The furnace was then heated up with a ramp rate of 35 °C/min to the growth temperatures (750 to 850 °C). The Sulphur component melted at 150 °C was sent into the furnace at the growth temperature to grow h-WS_2. The sample growth procedure proceeded for 10 minutes, after which the furnace was directly opened to room temperature to stop the reaction immediately.

Transfer of mono- and multilayer WS_2: Polystyrene (PS) was used as the supplementary film to peel off the WS_2 crystals from sapphire substrates. PS (M.W. 192000) dispersed in toluene solution (20 mg/mL) was spin-coated on top of the WS_2 sample at a speed of 3000 rpm. The edge of the PS film was scribed with a blade, and then the sample of PS/h-WS_2/Si-substrate was inserted into water slowly. The PS/h-WS_2 film became peeled off naturally in water, and was subsequently rinsed with deionized-water thrice before it was

picked up and placed onto the target substrate. The PS coating was removed with toluene after baking the sample at 80°C for 60 minutes.

Characterizations by atomic probe microscopy and Kelvin probe force microscopy

Atomic Force Microscopy (AFM) (Bruker Dimension Icon) under the tapping mode was applied to characterize the surface morphology of the WS_2 film transferred onto the SiO_2/Si substrate. The Kelvin probe force microscopy (KPFM) measurements were conducted on a Bruker Dimension Icon SPM. Doped silicon PFQNE-AL probes (Bruker) with a probe radius of 5 nm and a spring constant of 0.8 N/m were used for the electrical measurements.

Spectroscopic characterization

The quality of the WS_2 film was characterized using Raman spectroscopy, PL measurements, X-ray photoemission spectroscopy (XPS), and Ultraviolet photoemission spectroscopy (UPS). The Raman spectra were taken with a Renishaw M1000 and Renishaw InVia Raman spectrometer system using a 514.3 nm laser (2.41 eV) as the

excitation source. A 50× objective lens with a numerical aperture of 0.75 and a 2400 lines/mm and 1800 lines/mm grating were chosen during the measurement to achieve better signal-to-noise ratio. XPS and UPS studies were performed under ultra-high vacuum (residual gas pressure 5 ×10^{-9} torr) with a Kratos AXIS Ultra DLD and a magnetic immersion lens that consisted of a spherical mirror and concentric hemispherical analyzers with a delay-line detector (DLD). An Al Kα (1.486 KeV) monochromatic source and He 1 (21.2 eV) source were used as excitation sources for the XPS and UPS measurements, respectively. Ejected electrons were collected at a 90° angle from the horizontal. The time-resolved PL measurements were taken on an inverted microscope (Zeiss Axio Observer) equipped with an avalanche photodiode (Picoquant PDM series with PicoHarp 300 timing electronics). For the PL lifetime measurements, a 400 nm picosecond laser diode (70 ps pulse duration, 40 MHz repetition rate; PicoQuant) excitation source was used, and a 400 nm band pass filter was placed after laser source to purify the laser beam. A 100× objective lens with a numerical aperture of 0.9 (Zeiss, Inc.) was used to focus the pulsed laser to a small spot of 1.6 × 10^{-6} cm^2 with an estimated peak power density of 7.5 kW cm^{-2}.

STM/STS sample preparation and measurements

For the STM/STS studies, we transferred many flakes of WS_2 (with lateral dimensions of all grains greater than 10 μm) onto a commercial substrate with an atomic flat layer of Au (111) (200 nm thick) on mica so that the surface of the Au (111) / mica substrate was almost fully covered by monolayer WS_2 single crystals. The WS_2 / Au (111) / mica sample was annealed and sealed in vacuum, and then loaded onto our Omicron VT STM system. The base pressure of the system was 2×10^{-11} torr. Atomically resolved topographic and spectroscopic measurements were carried out on monolayer WS_2 samples at room temperature using a Pt/Ir STM tip.

ACKNOWLEDGEMENTS

The authors gratefully acknowledge joint support from the Army Research Office under the Multi-University Research Initiative (MURI) program, National Science Foundation under the Physics Frontier Center program for Institute for Quantum Information and Matter (IQIM), and Kavli Foundation. The authors thank Teddy Huang from the Bruker Nano Surface Company for helpful input regarding the CAFM data analysis, and Yen-Chun Chen for useful discussion on the CVD growth for TMDCs. The authors also acknowledge support from the Beckman Institute at the California Institute of Technology for access to facilities at the Molecular Materials Research Center.

ASSOCIATED CONTENT

Supporting Information

The Supporting Information is available free of charge on the ACS Publications website.

Supplementary Information Note 1 and Figures S1 and S2: CVD synthesis of monolayer WS_2 single crystals; Note 2 and Figure S3: Characteristic Raman mode

associated with defects/disorder in monolayer WS_2 single crystals; Note 3 and Figure S4: XPS and UPS surface characterizations of WS_2 single crystals; Note 4 and Figure S5: Circularly polarized emission from as-grown monolayer h-WS_2 under σ_- 514.3nm excitation. Note 5 and Figure S6: Circularly polarized emission from as-grown monolayer triangular shape WS_2 under σ_+ 514.3 nm excitation; Note 6: Theoretical derivations for the circular polarization P_{circ} of neutral excitons in the steady-state rate model; Note 7, Tables S1 and S2, and Figures S7: Summary of the degree of polarization in MoS_2 and WS_2 at room temperature and 80 K.

AUTHOR CONTRIBUTIONS

W.-H. Lin and N.-C. Yeh conceived the research ideas. W.-H. Lin construct the CVD system for h-WS_2 growth and participated in all the measurements and data analysis. W.-S. Tseng contributed to the XPS measurement. C. M. Went and H. A. Atwater contributed to the TRPL measurement. G. R. Rossman contributed to the Raman and PL mapping measurements. W.-H. Lin and H. A. Atwater contributed to the STM/STS studies presented in this manuscript using an Omicron VT STM system. M. L. Teague contributed

to the STM/STS studies with a homemade STM system in N.-C. Yeh's group to independently verify the STM/STS results obtained by the Omicron VT STM system. W.-H. Lin and N.-C. Yeh wrote the manuscript, and N.-C. Yeh supervised and coordinated the project.

COMPETING FINANCIAL INTERESTS

The authors declare no competing financial interests.

FIGURES

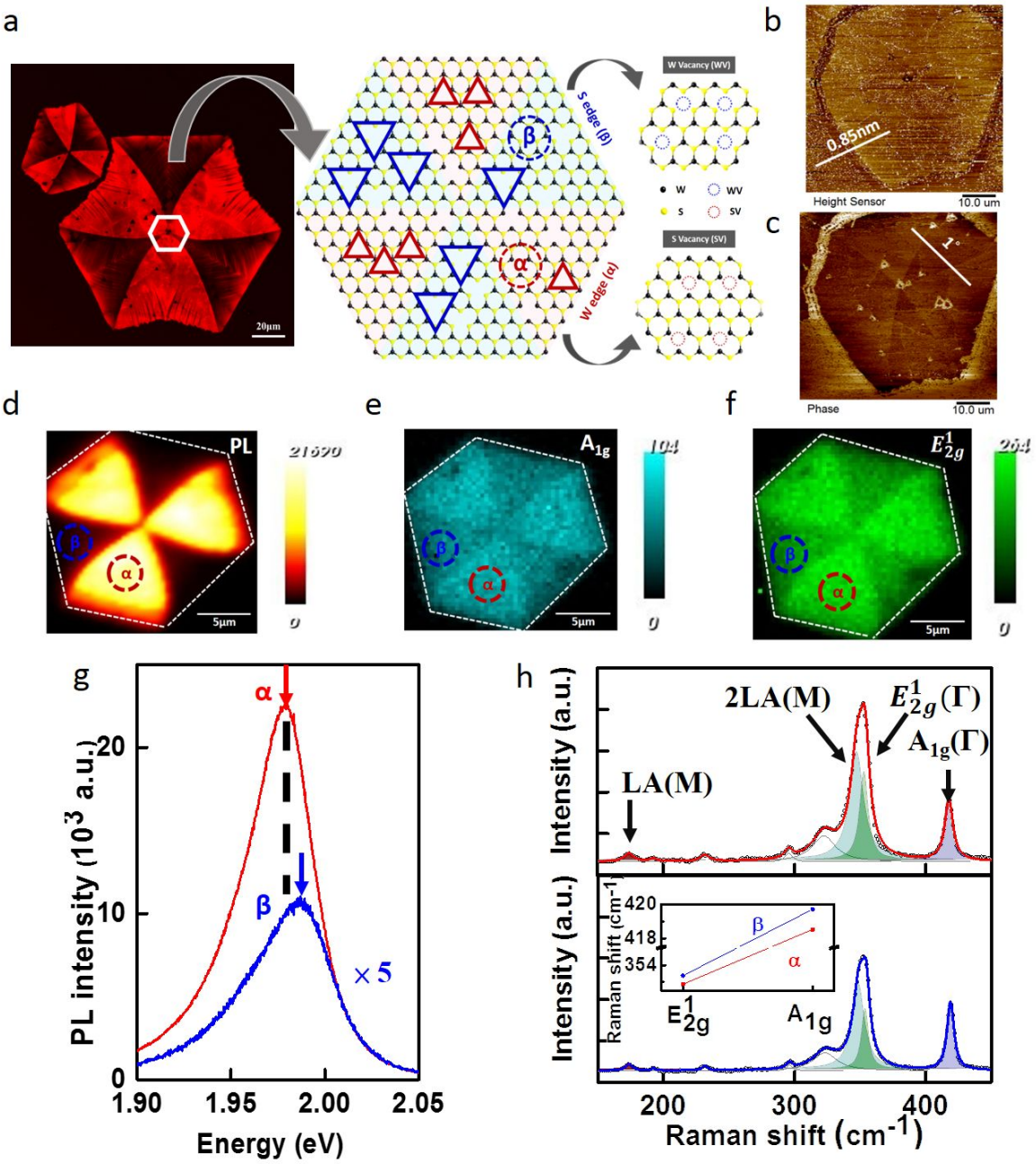
a
b
c
d
e
f
g
h
20μm
S edge (β)
W edge (α)
W Vacancy (WV)
S Vacancy (SV)
W
WV
S
SV
0.85nm
Height Sensor
10.0 um
1°
Phase
10.0 um
PL
21679
0
5μm
A1g
104
0
5μm
E12g
264
0
5μm
α
β
PL intensity (10^3 a.u.)
20
10
0
1.90
1.95
2.00
2.05
Energy (eV)
× 5
2LA(M)
E12g(Γ)
A1g(Γ)
LA(M)
Intensity (a.u.)
Raman shift (cm-1)
420
418
354
E12g
A1g
200
300
400
Raman shift (cm-1)

Figure 1. Monolayer h-WS_2 optical characterizations: **(a)** Left panel: Fluorescence images showing a radioactive hazard symbol-like optical emission pattern in the fluorescence intensity from a CVD-grown large monolayer WS_2 single crystal. Right panel: Schematic illustration of heterogeneous defect domains in single crystalline hexagonal WS_2. AFM measurements of **(b)** the surface topography and **(c)** the phase for a monolayer h-WS_2 single crystal. The scale bar is 10μm. **(d)** PL intensity mapping of a monolayer h-WS_2 single crystal at the PL peak energy of 1.96 eV. The brighter PL domain (α) and darker PL domain (β) show threefold symmetry. Similar symmetries are also found in the Raman spectral intensity mapping for **(e)** the A_{1g} mode and **(f)** the E^1_{2g} mode. Here the scale bars for (d-f) correspond to 5μm. **(g)** Representative PL point spectra for the α- and β-domains of a monolayer h-WS_2. **(h)** Representative Raman spectra for the corresponding α- and β-domains as in (e) and (f).

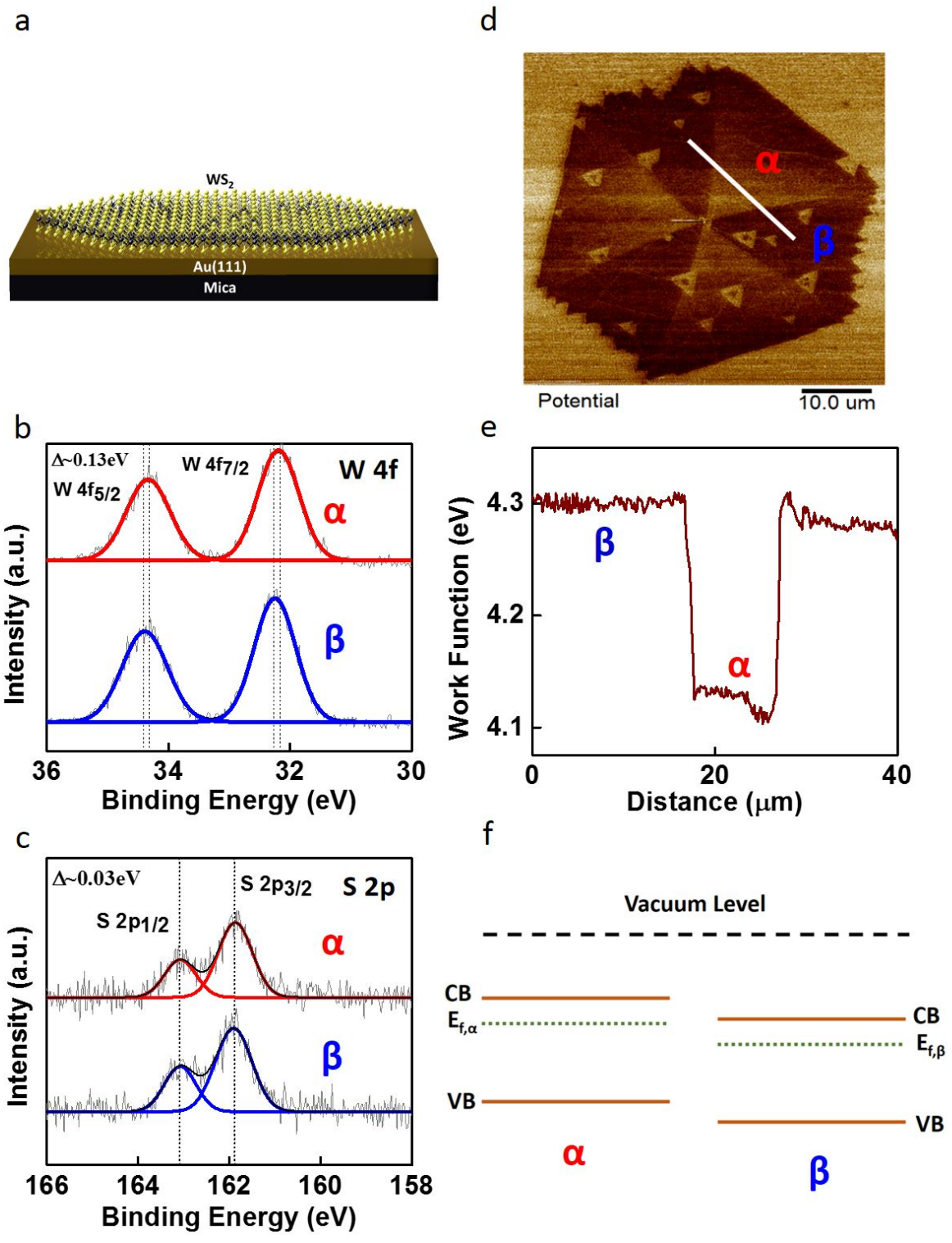
a
WS2
Au(111)
Mica
d
α
β
Potential
10.0 um
b
Δ~0.13eV
W 4f7/2
W 4f5/2
W 4f
α
β
Intensity (a.u.)
36
34
32
30
Binding Energy (eV)
e
4.3
4.2
4.1
Work Function (eV)
β
α
0
20
40
Distance (μm)
c
Δ~0.03eV
S 2p3/2
S 2p1/2
S 2p
α
β
Intensity (a.u.)
166
164
162
160
158
Binding Energy (eV)
f
Vacuum Level
CB
Ef,α
VB
α
CB
Ef,β
VB
β

Figure 2. Chemical bonding and work function characterization in heterogeneous domains: **(a)** Schematic of the monolayer h-WS_2 on Au (111) / mica substrate. Selected XPS spectra of the α-domain (top) and β-domain (bottom) for **(b)** W-4f and **(c)** S-2p, showing an upshift by ~ 0.13 eV (~ 0.03 eV) in the W-4f (S-2p) peaks of the α-domain relative to those of the β-domain. The error range for the binding energies determined by our XPS system is ±0.025 eV. **(d)** KPFM image of the heterogeneous domains of a monolayer h-WS_2. **(e)** Work function plot along the white line in (d). **(f)** Estimated Fermi levels ($E_{f,\alpha}$ and $E_{f,\beta}$) and the corresponding conduction band (CB) and valence band (VB) positions of the α- and β-domains with respect to the vacuum level based on KPFM.

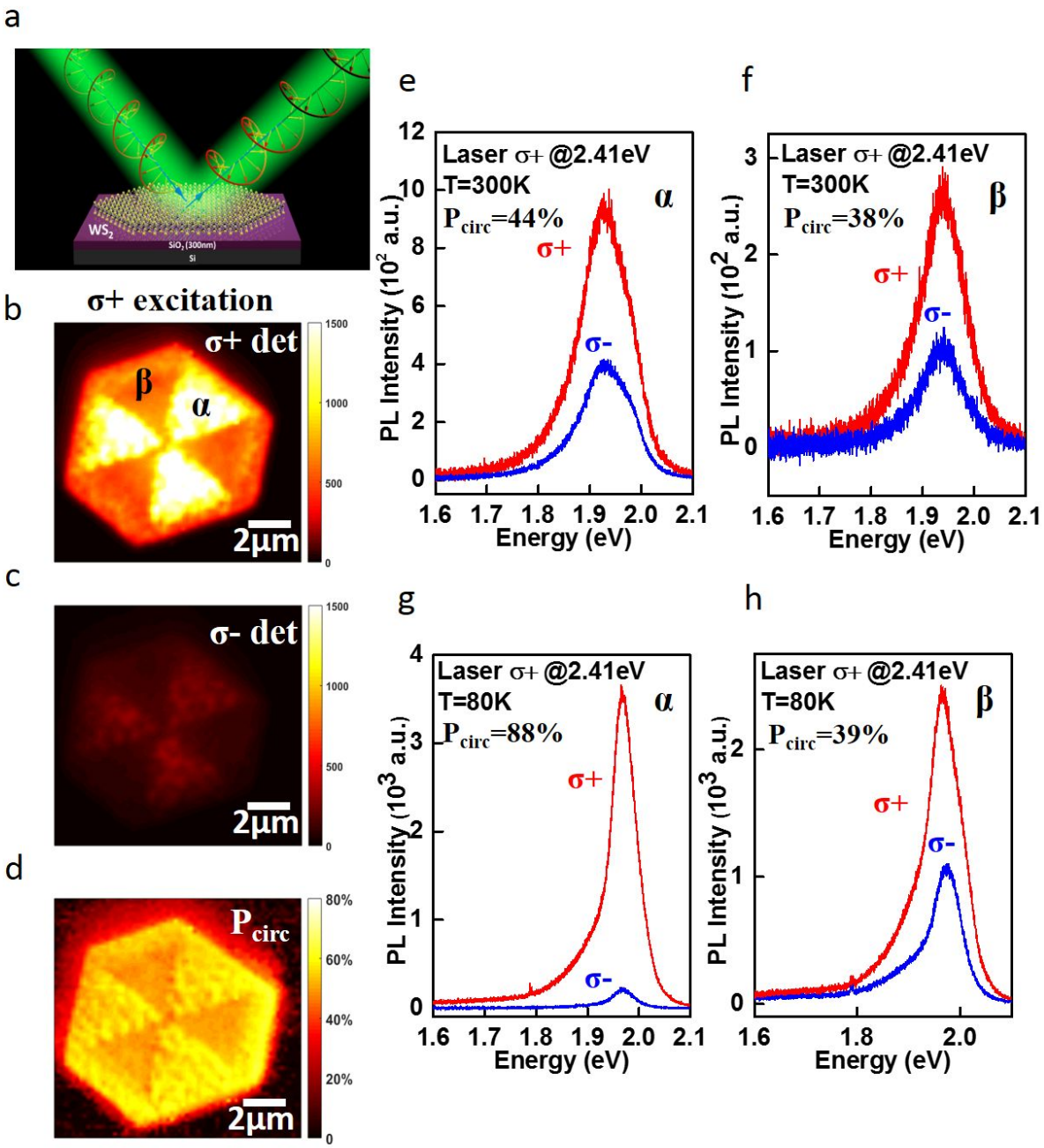
a
WS2
SiO2 (300nm)
Si
b
σ+ excitation
σ+ det
β
α
2μm
1500
1000
500
0
c
σ- det
2μm
d
Pcirc
2μm
80%
60%
40%
20%
0
e
Laser σ+ @2.41eV
T=300K
Pcirc=44%
α
σ+
σ-
PL Intensity (10^2 a.u.)
Energy (eV)
f
Laser σ+ @2.41eV
T=300K
Pcirc=38%
β
σ+
σ-
PL Intensity (10^2 a.u.)
Energy (eV)
g
Laser σ+ @2.41eV
T=80K
Pcirc=88%
α
σ+
σ-
PL Intensity (10^3 a.u.)
Energy (eV)
h
Laser σ+ @2.41eV
T=80K
Pcirc=39%
β
σ+
σ-
PL Intensity (10^3 a.u.)
Energy (eV)

Figure 3. Circularly-polarized emission of monolayer h-WS_2 neutral excitons: **(a)** Schematic of circularly polarized emission on monolayer h-WS_2 under σ_+ 514nm (2.41 eV) excitation. **(b)** An intensity map for the σ_+ polarized emission and **(c)** an intensity map for the σ_- polarized emission. **(d)** A spatial map for the degree of valley polarization P_{circ} in a monolayer h-WS_2 single crystal. **(e-f)** Representative σ_+ (red) and σ_- (blue) PL intensity spectra taken at room temperature on the α- and β-domains, respectively. **(g-h)** Representative σ_+ (red) and σ_- (blue) PL intensity spectra taken at 80 K on the α- and β-domains, respectively.

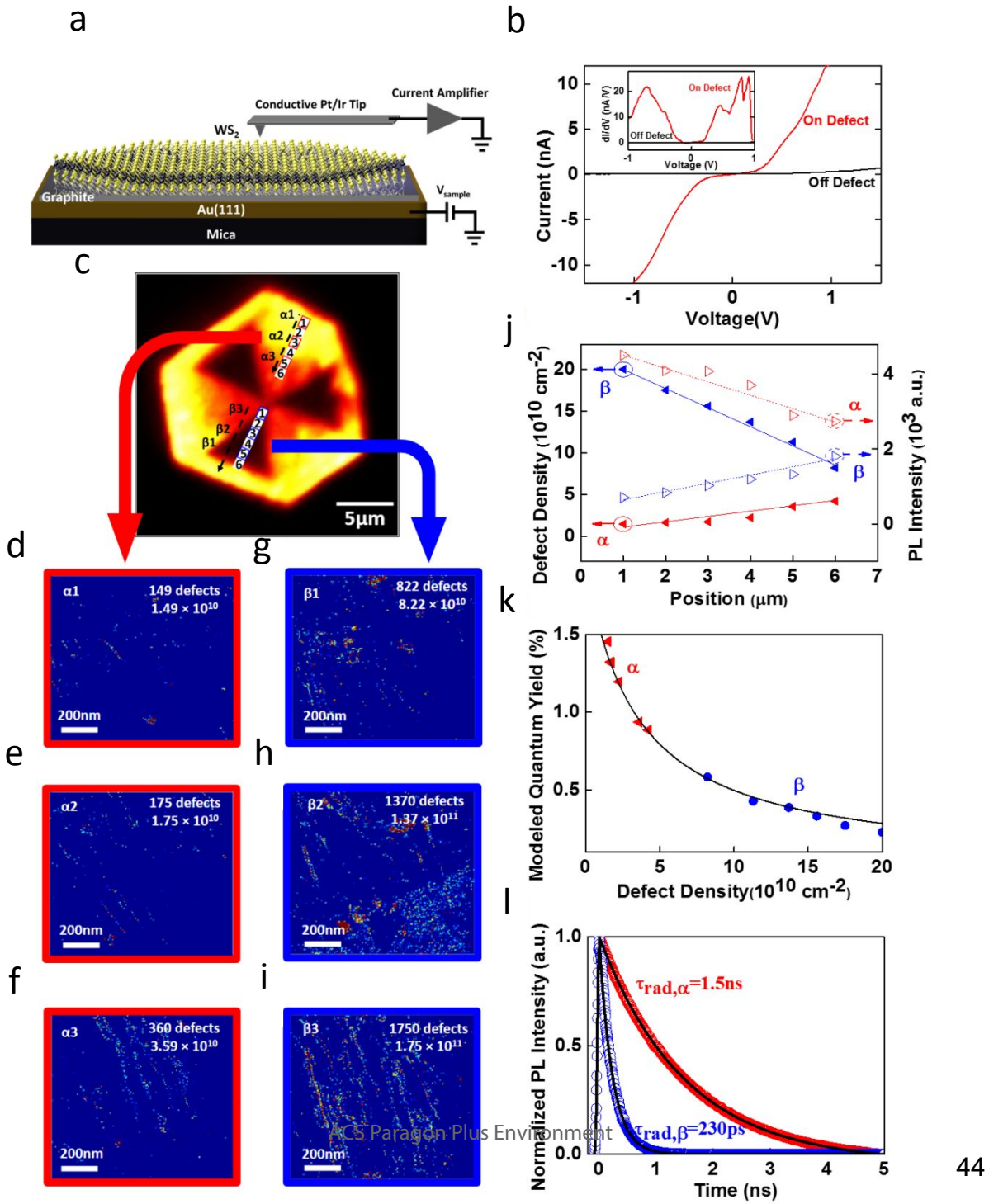

Figure 4. Electrical characterizations of the monolayer h-WS_2: **(a)** Schematic illustration of the experimental setup for the CAFM measurements. A CVD-grown thick multilayer graphene sample was transferred onto an atomically flat Au (111) / mica substrate to provide a conductive backplane for the measurement. A monolayer h-WS_2 sample was subsequently transferred onto the thick multilayer graphene using the transfer method described in Methods. **(b)** I-V curves taken on a defect and off a defect, showing a drastic difference in the conduction characteristics between a defect region and the pristine h-WS_2. The inset figure in (b) shows the dI/dV characteristics corresponding to the I-V curve in the main panel of (b). **(c)** PL map of the h-WS_2 sample, with numbers 1 through 6 labeled in both one of the α-domains and one of the β-domains. The numbers correspond to the locations where detailed CAFM maps were taken. **(d-i)** CAFM measurements of the locations (α_1, α_2, α_3, β_1, β_2, β_3) labeled in (c), exhibiting defect densities in the α-domain: **(d)** 1.49×10^{10} cm^{-2} for α_1, **(e)** 1.75×10^{10} cm^{-2} for α_2, **(f)** 3.59×10^{10} cm^{-2} for α_3, and in the β-domain: **(g)** 8.22×10^{10} cm^{-2} for β_1, **(h)** 1.37×10^{11} cm^{-2} for β_2, **(i)** 1.75×10^{11} cm^{-2} for β_3. **(j)** Defect density and PL intensity as a function of position along the dashed line shown in (c) across the α- and β-domains, showing apparent anti-correlation between the defect density and the PL intensity. **(k)** The model presented in Eq. (7). The red points correspond to the PL measurements of the α-domain, and blue points correspond to the PL measurements of the β-domain. **(l)** TRPL results, showing PL decay profiles of the α- and β-domains. The black lines are fitting curves using a single exponential decay function.

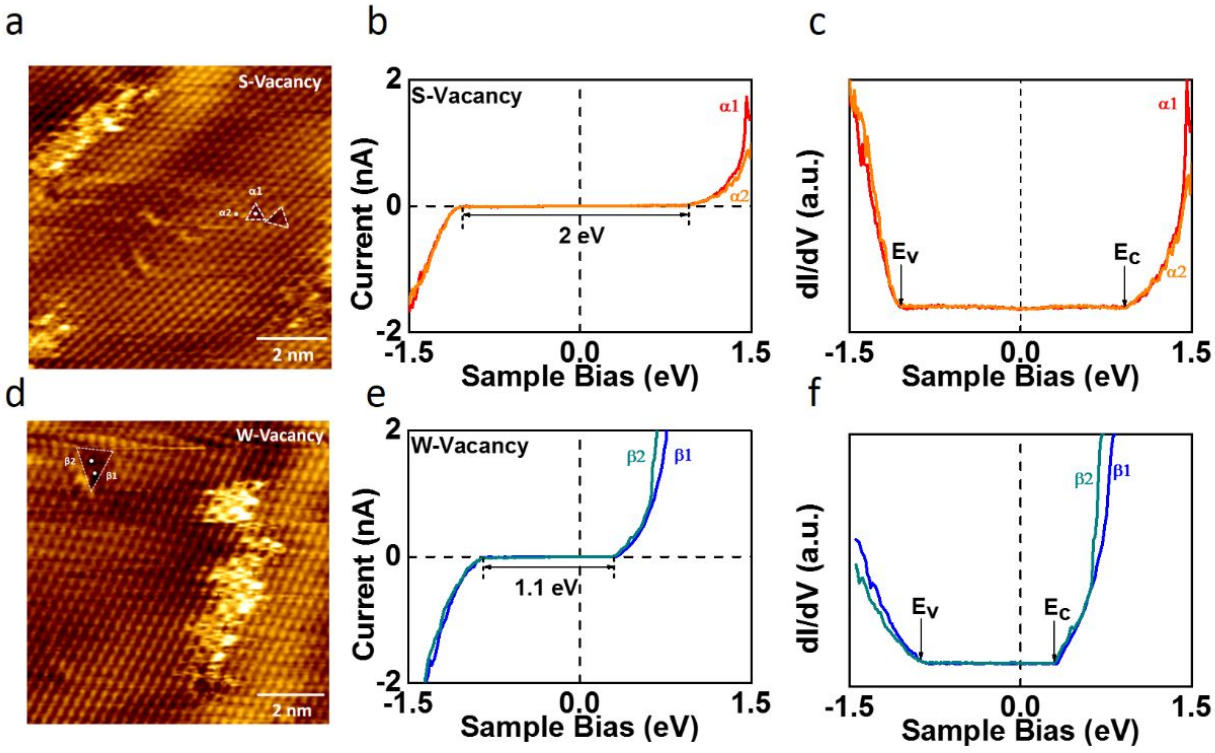

Figure 5. Scanning tunneling microscopic and spectroscopic studies of WS_2 monolayer: (**a**) Atomically-resolved of SVs (as indicated by the white triangles) on a sample of monolayer WS_2 on Au substrate. The topography was recorded under 0.7V, 1.2nA. Here the white solid circle $\alpha 1$ refers to the location of a SV in the center of a white triangle, and the white solid circle $\alpha 2$ refers to the location of a vacancy-free region. (**b**) Tunneling current (I) vs. sample biased voltage (V) spectra taken at a SV ($\alpha 1$) and defect free region ($\alpha 2$), showing consistent energy gaps of ~ 2.0 eV. Here the vertical dashed line corresponds to $E = 0$ (the Fermi level). (**c**) (dI/dV)-*vs.*-V spectra obtained from the regions $\alpha 1$ and $\alpha 2$ shown in (**a**). (**d**) Atomically-resolved WVs (shown by the white triangle) on a sample of monolayer WS_2 on Au substrate, with the topography recorded under 0.7V, 1.2nA. (**e**) I-*vs.*-V spectra taken at two WVs (white solid circles $\beta 1$ and $\beta 2$ in (d)), showing a reduced energy gap of 1.1 eV. The vertical dashed line corresponds to $E = 0$ (the Fermi level). (**f**) (dI/dV)-*vs.*-V spectra obtained from the regions $\beta 1$ and $\beta 2$ shown in (d). The tunneling spectra associated with the WVs are qualitatively similar to the CAFM measurements at non-radiative defect sites, suggesting that the WVs are responsible for the non-radiative defects that suppress PL and DOP in h-WS_2.

TOC Figure.

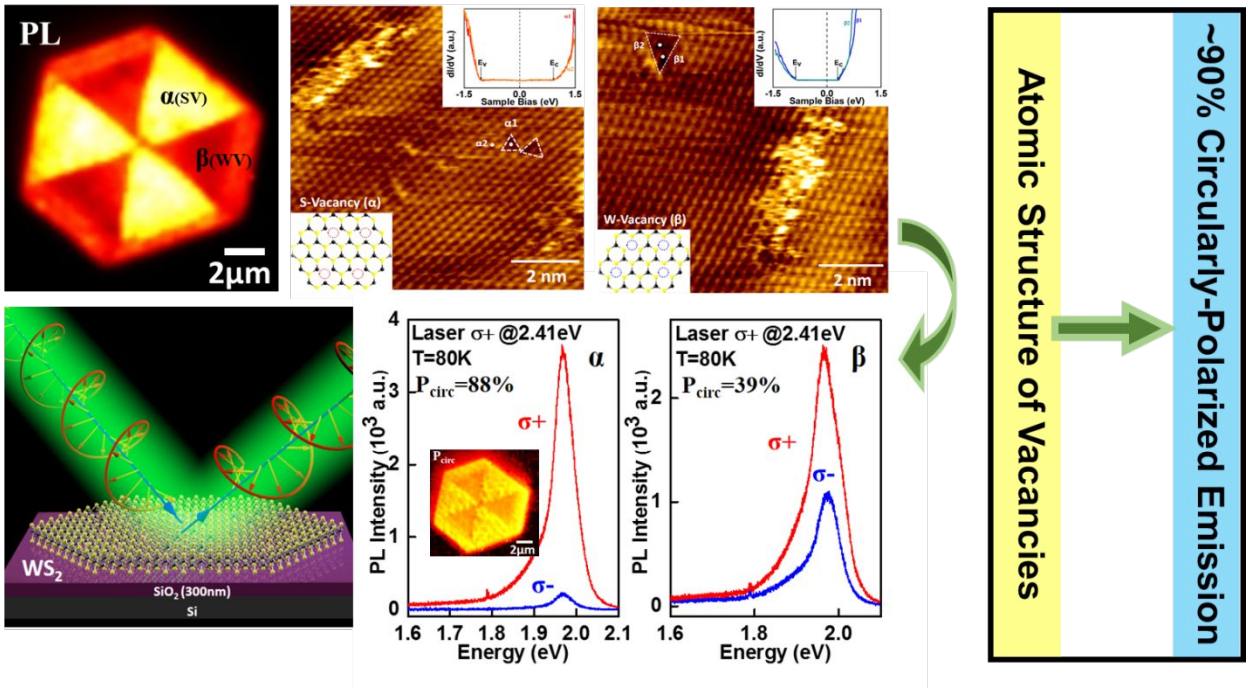
PL
α(SV)
β(WV)
2μm
S-Vacancy (α)
2 nm
W-Vacancy (β)
2 nm
WS2
SiO2 (300nm)
Si
Laser σ+ @2.41eV
T=80K
Pcirc=88%
α
σ+
σ-
PL Intensity (10^3 a.u.)
Energy (eV)
Laser σ+ @2.41eV
T=80K
Pcirc=39%
β
σ+
σ-
PL Intensity (10^3 a.u.)
Energy (eV)
Atomic Structure of Vacancies
~90% Circularly-Polarized Emission

REFERENCES

1. Novoselov, K. S.; Jiang, D.; Schedin, F.; Booth, T. J.; Khotkevich, V. V.; Morozov, S. V.; Geim, A. K. Two-Dimensional Atomic Crystals. *P. Natl. Acad. Sci. USA* **2005**, 102, 10451-10453.

2. Novoselov, K. S.; Mishchenko, A.; Carvalho, A.; Neto, A. H. C. 2D Materials and van der Waals Heterostructures. *Science* **2016**, 353, 6298.

3. Mas-Balleste, R.; Gomez-Navarro, C.; Gomez-Herrero, J.; Zamora, F. 2D Materials: To Graphene and Beyond. *Nanoscale* **2011**, 3, 20-30.

4. Wang, F.; Wang, Z. X.; Yin, L.; Cheng, R. Q.; Wang, J. J.; Wen, Y.; Shifa, T. A.; Wang, F. M.; Zhang, Y.; Zhan, X. Y.; He, J. 2D Library Beyond Graphene and Transition Metal Dichalcogenides: A Focus on Photodetection. *Chem. Soc. Rev.* **2018**, 47, 6296-6341.

5. Geim, A. K. & Novoselov, K. S. The Rise of Graphene. *Nat. Mater.* **2007**, 6 , 183-191.

6. Novoselov, K. S. Nobel Lecture: Graphene: Materials in the Flatland. *Rev. Mod. Phys.* **2011**, 83, 837-849.

7. Sheng, Y. W.; Rong, Y. M.; He, Z. Y.; Fan, Y.; Warner, J. H. Uniformity of Large-Area Bilayer Graphene Grown by Chemical Vapor Deposition. *Nanotechnology* **2015**, 26, 395601.

8. Boyd, D. A.; Lin, W.-H.; Hsu, C.-C.; Teague, M. L.; Chen, C. C.; Lo, Y. Y.; Chan, W. Y.; Su, W. B.; Cheng, T. C.; Chang, C. S.; Wu, C.-I.; Yeh, N.-C. Single-Step Deposition of High-Mobility Graphene at Reduced Temperatures. *Nat. Commun.* **2015**, 6, 6620.

9. Lin, W.-H.; Chen, T. H.; Chang, J. K.; Taur, J. I.; Lo, Y. Y.; Lee, W. L.; Chang, C. S.; Su, W. B.; Wu, C.-I. A Direct and Polymer-Free Method for Transferring Graphene

Grown by Chemical Vapor Deposition to Any Substrate. *ACS Nano* **2014**, 8, 1784-1791.

10. Gao, T.; Song, X. J.; Du, H. W.; Nie, Y. F.; Chen, Y. B.; Ji, Q. Q.; Sun, J. Y.; Yang, Y. L.; Zhang, Y. F.; Liu, Z. F. Temperature-Triggered Chemical Switching Growth of In-Plane and Vertically Stacked Graphene-Boron Nitride Heterostructures. *Nat. Commun.* **2015**, 6, 6835.

11. Dean, C. R.; Young, A. F.; Meric, I.; Lee, C.; Wang, L.; Sorgenfrei, S.; Watanabe, K.; Taniguchi, T.; Kim, P.; Shepard, K. L.; Hone, J. Boron Nitride Substrates for High-Quality Graphene Electronics. *Nat. Nanotechnol.* **2010**, 5, 722-726.

12. Ci, L.; Song, L.; Jin, C. H.; Jariwala, D.; Wu, D. X.; Li, Y. J.; Srivastava, A.; Wang, Z. F.; Storr, K.; Balicas, L.; Liu, F.; Ajayan, P. M. Atomic Layers of Hybridized Boron Nitride and Graphene Domains. *Nat. Mater.* **2010**, 9, 430-435.

13. Kim, K. K.; Hsu, A.; Jia, X. T.; Kim, S. M.; Shi, Y. S.; Hofmann, M.; Nezich, D.; Rodriguez-Nieva, J. F.; Dresselhaus, M. S.; Palacios, T.; Kong, J. Synthesis of Monolayer Hexagonal Boron Nitride on Cu Foil Using Chemical Vapor Deposition. *Nano Lett.* **2012**, 12, 161-166.

14. Lin, W.-H.; Brar, V. W.; Jariwala, D.; Sherrott, M. C.; Tseng, W.-S.; Wu, C.-I.; Yeh, N.-C.; Atwater, H. A. Atomic-Scale Structural and Chemical Characterization of Hexagonal Boron Nitride Layers Synthesized at the Wafer-Scale with Monolayer Thickness Control. *Chem. Mater.* **2017**, 29, 4700-4707.

15. Fang, H.; Chuang, S.; Chang, T. C.; Takei, K.; Takahashi, T.; Javey, A. High-Performance Single Layered WSe_2 *p*-FETs with Chemically Doped Contacts. *Nano Lett.* **2012**, 12, 3788-3792.

16. Wang, H,; Yu, L. L.; Lee, Y. H.; Shi, Y. M.; Hsu, A.; Chin, M. L.; Li, L. J.; Dubey, M.; Kong, J. & Palacios, T. Integrated Circuits Based on Bilayer MoS_2 Transistors. *Nano Lett.* **2012**, 12, 4674-4680.

17. Zeng, H. L.; Dai, J. F.; Yao, W.; Xiao, D. & Cui, X. D. Valley Polarization in MoS_2 Monolayers by Optical Pumping. *Nat. Nanotechnol.* **2012**, 7, 490-493.

18. Jones, A. M.; Yu, H. Y.; Ghimire, N. J.; Wu, S. F.; Aivazian, G.; Ross, J. S.; Zhao, B.; Yan, J. Q.; Mandrus, D. G.; Xiao, D.; Yao, W.; Xu, X. D. Optical Generation of Excitonic Valley Coherence in Monolayer WSe_2. *Nat. Nanotechnol.* **2013**, 8, 634-638.

19. He, Z. Y.; Sheng, Y. W.; Rong, Y. M.; Lee, G. D.; Li, J.; Warner, J. H. Layer-Dependent Modulation of Tungsten Disulfide Photoluminescence by Lateral Electric Fields. *ACS Nano* **2015,** 9, 2740-2748.

20. Kim, I. S.; Sangwan, V. K.; Jariwala, D.; Wood, J. D.; Park, S.; Chen, K. S.; Shi, F. Y.; Ruiz-Zepeda, F.; Ponce, A.; Jose-Yacaman, M.; Dravid, V. P.; Marks, T. J.; Hersam, M. C.; Lauhon, L. J. Influence of Stoichiometry on the Optical and Electrical Properties of Chemical Vapor Deposition Derived MoS_2. *ACS Nano* **2014,** 8, 10551-10558.

21. Han, H. V.; Lu, A. Y.; Lu, L. S.; Huang, J. K.; Li, H. N.; Hsu, C. L.; Lin, Y. C.; Chiu, M. H.; Suenaga, K.; Chu, C. W.; Kuo, H. C.; Chang, W. H.; Li, L. J.; Shi, Y. M. Photoluminescence Enhancement and Structure Repairing of Monolayer $MoSe_2$ by Hydrohalic Acid Treatment. *ACS Nano* **2016,** 10, 1454-1461.

22. Li, H.; Tsai, C.; Koh, A. L.; Cai, L. L.; Contryman, A. W.; Fragapane, A. H.; Zhao, J. H.; Han, H. S.; Manoharan, H. C.; Abild-Pedersen, F.; Norskov, J. K.; Zheng, X. L. Activating and Optimizing MoS_2 Basal Planes for Hydrogen Evolution Through the Formation of Strained Sulphur Vacancies. *Nat. Mater.* **2016**, 15, 48.

23. Jeong, H. Y.; Jin, Y.; Yun, S. J.; Zhao, J.; Baik, J.; Keum, D. H.; Lee, H. S.; Lee, Y. H. Heterogeneous Defect Domains in Single-Crystalline Hexagonal WS_2. *Adv. Mater.* **2017**, 29, 1605043.

24. Lin, Y. C.; Li, S. S.; Komsa, H. P.; Chang, L. J.; Krasheninnikov, A. V.; Eda, G. K.; Suenaga, K. Revealing the Atomic Defects of WS_2 Governing Its Distinct Optical Emissions. *Adv. Funct. Mater.* **2018**, 28, 1704210.

25. Ly, T. H.; Yun, S. J.; Thi, Q. H.; Zhao, J. Edge Delamination of Monolayer Transition Metal Dichalcogenides. *ACS Nano* **2017**, 11, 7534-7541.

26. Sheng, Y. W.; Wang, X. C.; Fujisawa, K.; Ying, S. Q.; Elias, A. L.; Lin, Z.; Xu, W. S.; Zhou, Y. Q.; Korsunsky, A. M.; Bhaskaran, H.; Terrones, M.; Warner, J. H. Photoluminescence Segmentation within Individual Hexagonal Monolayer Tungsten Disulfide Domains Grown by Chemical Vapor Deposition. *ACS Appl. Mater. Inter.* **2017**, 9, 15005-15014.

27. Kumar, P.; Verma, N. C.; Goyal, N.; Biswas, J.; Lodha, S.; Nandi, C. K.; Balakrishnan, V. Phase Engineering of Seamless Heterophase Homojunctions with Co-Existing 3R and 2H Phases in WS_2 Monolayers. *Nanoscale* **2018**, 10, 3320-3330.

28. Kormanyos, A.; Burkard, G.; Gmitra, M.; Fabian, J.; Zolyomi, V.; Drummond, N. D.; Fal'ko, V. $k \cdot p$ Theory for Two-Dimensional Transition Metal Dichalcogenide Semiconductors. *2D Mater.* **2015**, 2, 022001.

29. Ulstrup, S.; Katoch, J.; Koch, R. J.; Schwarz, D.; Singh, S.; McCreary, K. M.; Yoo, H. K.; Xu, J. S.; Jonker, B. T.; Kawakami, R. K.; Bostwick, A.; Rotenberg, E.; Jozwiak, C. Spatially Resolved Electronic Properties of Single-Layer WS_2 on Transition Metal Oxides. *ACS Nano* **2016**, 10, 10058-10067.

30. Mak, K. F.; He, K.; Shan, J.; Heinz, T. F. Control of Valley Polarization in Monolayer MoS_2 by Optical Helicity. *Nat. Nanotechnol.* **2012**, 7, 494.

31. Kioseoglou, G.; Hanbicki, A. T.; Currie, M.; Friedman, A. L.; Gunlycke, D.; Jonker, B. T. Valley Polarization and Intervalley Scattering in Monolayer MoS_2. *Appl. Phys. Lett.* **2012**, 101, 221907.

32. Cao, T.; Wang, G.; Han, W. P.; Ye, H. Q.; Zhu, C. R.; Shi, J. R.; Niu, Q.; Tan, P. H.; Wang, E.; Liu, B. L.; Feng, J. Valley-Selective Circular Dichroism of Monolayer Molybdenum Disulphide. *Nat. Commun.* **2012**, 3, 887.

33. Yu, T.; Wu, M. W. Valley Depolarization due to Intervalley and Intravalley Electron-Hole Exchange Interactions in Monolayer MoS_2. *Phys. Rev. B* **2014**, 89, 205303.

34. Zhu, C. R.; Zhang, K.; Glazov, M.; Urbaszek, B.; Amand, T.; Ji, Z. W.; Liu, B. L.; Marie, X. Exciton Valley Dynamics Probed by Kerr Rotation in WSe_2 Monolayers. *Phys. Rev. B* **2014**, 90, 161302.

35. Mai, C.; Semenov, Y. G.; Barrette, A.; Yu, Y. F.; Jin, Z. H.; Cao, L. Y.; Kim, K. W.; Gundogdu, K. Exciton Valley Relaxation in a Single Layer of WS_2 Measured by Ultrafast Spectroscopy. *Phys. Rev. B* **2014**, 90, 041414.

36. Kioseoglou, G.; Hanbicki, A. T.; Currie, M.; Friedman, A. L.; Jonker, B. T. Optical Polarization and Intervalley Scattering in Single Layers of MoS_2 and $MoSe_2$. *Sci. Rep.* **2016**, 6, 25041.

37. Wu, S. F.; Huang, C. M.; Aivazian, G.; Ross, J. S.; Cobden, D. H.; Xu, X. D. Vapor-Solid Growth of High Optical Quality MoS_2 Monolayers with Near-Unity Valley Polarization. *ACS Nano* **2013**, 7, 2768-2772.

38. Sallen, G.; Bouet, L.; Marie, X.; Wang, G.; Zhu, C. R.; Han, W. P.; Lu, Y.; Tan, P. H.; Amand, T.; Liu, B. L.; Urbaszek, B. Robust Optical Emission Polarization in MoS2 Monolayers Through Selective Valley Excitation. *Phys. Rev. B* **2012**, 86, 081301.

39. Lagarde, D.; Bouet, L.; Marie, X.; Zhu, C. R.; Liu, B. L.; Amand, T.; Tan, P. H.; Urbaszek, B. Carrier and Polarization Dynamics in Monolayer MoS_2. *Phys. Rev. Lett.* **2014**, 112, 047401.

40. Hanbicki, A. T.; Kioseoglou, G.; Currie, M.; Hellberg, C. S.; McCreary, K. M.; Friedman, A. L.; Jonker, B. T. Anomalous Temperature-Dependent Spin-Valley Polarization in Monolayer WS_2. *Sci. Rep.* **2016**, 6, 18885.

41. Zhu, B. R.; Zeng, H. L.; Dai, J. F.; Gong, Z. R.; Cui, X. D. Anomalously Robust Valley Polarization and Valley Coherence in Bilayer WS_2. *P. Natl. Acad. Sci. USA* **2014**, 111, 11606-11611.

42. Rosenberger, M. R.; Chuang, H. J.; McCreary, K. M.; Li, C. H.; Jonker, B. T. Electrical Characterization of Discrete Defects and Impact of Defect Density on Photoluminescence in Monolayer WS_2. *ACS Nano* **2018**, 12, 1793-1800.

43. McCreary, A.; Berkdemir, A.; Wang, J. J.; Nguyen, M. A.; Elias, A. L.; Perea-Lopez, N.; Fujisawa, K.; Kabius, B.; Carozo, V.; Cullen, D. A.; Mallouk, T. E.; Zhu, J.; Terrones, M. Distinct Photoluminescence and Raman Spectroscopy Signatures for Identifying Highly Crystalline WS_2 Monolayers Produced by Different Growth Methods. *J. Mater. Res.* **2016**, 31, 931-944.

44. Yu, Y. F.; Yu, Y. L.; Xu, C.; Cai, Y. Q.; Su, L. Q.; Zhang, Y.; Zhang, Y. W.; Gundogdu, K.; Cao, L. Y. Engineering Substrate Interactions for High Luminescence Efficiency of Transition-Metal Dichalcogenide Monolayers. *Adv. Funct. Mater.* **2016**, 26, 4733-4739.

45. Ceballos, F.; Bellus, M. Z.; Chiu, H. Y.; Zhao, H. Ultrafast Charge Separation and Indirect Exciton Formation in a MoS_2-$MoSe_2$ van der Waals Heterostructure. *ACS Nano* **2014**, 8, 12717-12724.

46. Wang, H.; Zhang, C.; Rana, F. Ultrafast Dynamics of Defect-Assisted Electron-Hole Recombination in Monolayer MoS_2. *Nano Lett.* **2015**, 15, 339-345.

47. Bhanu, U.; Islam, M. R.; Tetard, L.; Khondaker, S. I. Photoluminescence Quenching in Gold - MoS_2 Hybrid Nanoflakes". *Sci. Rep.* **2014**, 4, 5575.

48. Tongay, S.; Suh, J.; Ataca, C.; Fan, W.; Luce, A.; Kang, J. S.; Liu, J.; Ko, C.; Raghunathanan, R.; Zhou, J.; Ogletree, F.; Li, J. B.; Grossman, J. C.; Wu, J. Q. Defects Activated Photoluminescence in Two-Dimensional Semiconductors: Interplay between Bound, Charged, and Free Excitons". *Sci. Rep.* **2013**, 3, 2657.

49. Yuan, L. & Huang, L. B. Exciton Dynamics and Annihilation in WS_2 2D Semiconductors. *Nanoscale* **2015**, 7, 7402-7408.

50. Ceballos, F. & Zhao, H. Ultrafast Laser Spectroscopy of Two-Dimensional Materials Beyond Graphene. *Adv. Funct. Mater.* **2017**, 27, 2657.

51. McCreary, K. M.; Currie, M.; Hanbicki, A. T.; Chuang, H. J.; Jonker, B. T. Understanding Variations in Circularly Polarized Photoluminescence in Monolayer Transition Metal Dichalcogenides. *ACS Nano* **2017**, 11, 7988-7994.

52. Miller, B.; Steinhoff, A.; Pano, B.; Klein, J.; Jahnke, F.; Holleitner, A.; Wurstbauer, U. Long-Lived Direct and Indirect Interlayer Excitons in van der Waals Heterostructures. *Nano Lett* **2017,** 17, 5229-5237.

53. He, J. Q.; He, D. W.; Wang, Y. S.; Cui, Q. N.; Ceballos, F.; Zhao, H. Spatiotemporal Dynamics of Excitons in Monolayer and Bulk WS_2. *Nanoscale* **2015**, 7, 9526-9531.

54. Zhao, P.; Amani, M.; Lien, D. H.; Ahn, G. H.; Kiriya, D.; Mastandrea, J. P.; Ager, J. W.; Yablonovitch, E.; Chrzan, D. C.; Javey, A. Measuring the Edge Recombination Velocity of Monolayer Semiconductors. *Nano Lett.* **2017**, 17, 5356-5360.

55. Hanbicki, A. T.; Currie, M.; Kioseoglou, G.; Friedman, A. L.; Jonker, B. T. Measurement of High Exciton Binding Energy in the Monolayer Transition-Metal Dichalcogenides WS_2 and WSe_2. *Solid State Commun.* **2015**, 203, 16-20.

56. Amin, B.; Kaloni, T. P. & Schwingenschlögl, U. Strain Engineering of WS_2, WSe_2, and WTe_2. *RSC Adv.* **2014**, 4, 34561.